



## RESEARCH ARTICLE

10.1029/2022JB024443

### Key Points:

- We introduce a modified Coulomb Failure seismicity model in which a mean time-to-failure replaces instantaneous triggering
- The model explains the main features of time-dependent seismicity, including aftershock activity and stress shadow effects
- As a special case, it includes the rate-state model solutions but can also handle subcritical stresses and other fracture types

### Correspondence to:

T. Dahm,  
[dahm@gfz-potsdam.de](mailto:dahm@gfz-potsdam.de);  
[tdahm@uni-potsdam.de](mailto:tdahm@uni-potsdam.de)

### Citation:

Dahm, T., & Hainzl, S. (2022). A Coulomb stress response model for time-dependent earthquake forecasts. *Journal of Geophysical Research: Solid Earth*, 127, e2022JB024443. <https://doi.org/10.1029/2022JB024443>

Received 23 MAR 2022

Accepted 14 AUG 2022

### Author Contributions:

**Conceptualization:** Torsten Dahm  
**Investigation:** Torsten Dahm, Sebastian Hainzl  
**Methodology:** Torsten Dahm, Sebastian Hainzl  
**Software:** Torsten Dahm, Sebastian Hainzl  
**Validation:** Torsten Dahm, Sebastian Hainzl  
**Visualization:** Torsten Dahm, Sebastian Hainzl  
**Writing – original draft:** Torsten Dahm  
**Writing – review & editing:** Torsten Dahm, Sebastian Hainzl

# A Coulomb Stress Response Model for Time-Dependent Earthquake Forecasts

Torsten Dahm<sup>1,2</sup>  and Sebastian Hainzl<sup>1</sup> 

<sup>1</sup>GFZ German Research Centre for Geosciences, Physics of Earthquakes and Volcanoes, Potsdam, Germany, <sup>2</sup>Institute of Geosciences, University of Potsdam, Potsdam, Germany

**Abstract** Seismicity models are probabilistic forecasts of earthquake rates to support seismic hazard assessment. Physics-based models allow extrapolating previously unsampled parameter ranges and enable conclusions on underlying tectonic or human-induced processes. The Coulomb Failure (CF) and the rate-and-state (RS) models are two widely used physics-based seismicity models both assuming pre-existing populations of faults responding to Coulomb stress changes. The CF model depends on the absolute Coulomb stress and assumes instantaneous triggering if stress exceeds a threshold, while the RS model only depends on stress changes. Both models can predict background earthquake rates and time-dependent stress effects, but the RS model with its three independent parameters can additionally explain delayed aftershock triggering. This study introduces a modified CF model where the instantaneous triggering is replaced by a mean time-to-failure depending on the absolute stress value. For the specific choice of an exponential dependence on stress and a stationary initial seismicity rate, we show that the model leads to identical results as the RS model and reproduces the Omori-Utsu relation for aftershock decays as well stress-shadowing effects. Thus, both CF and RS models can be seen as special cases of the new model. However, the new stress response model can also account for subcritical initial stress conditions and alternative functions of the mean time-to-failure depending on the problem and fracture mode.

**Plain Language Summary** One of the most pressing questions in earthquake physics is understanding where and when earthquakes occur and how seismicity is related to stress changes in the Earth's crust. This question is even more important today because humans are increasingly influencing stresses in the Earth by exploiting the subsurface. So far, two classes of physics-based seismicity models have been used primarily. One assumes instantaneous earthquake occurrence when stress exceeds a threshold, and the other is based on the nucleation of earthquakes according to friction laws determined in the laboratory. Both models are very different in their approaches, have advantages and disadvantages, and are limited in their applicability. In this paper, we introduce a new concept of seismicity models, which is very simple and short to derive and combines the strengths of both previous models, as shown in various applications to human-related seismicity. The forecasts of both traditional models turn out to be special cases of the new model.

## 1. Introduction

A seismicity model describes the occurrence of earthquakes, that is, their origin times, locations, and magnitudes. Because of the complexity of the earthquake processes, nearly all seismicity models use statistical components and only predict the average earthquake rate, respectively the occurrence probability, of earthquakes. Because seismicity models are the backbone of probabilistic seismic hazard assessments, a useful model must be able to represent real seismicity reliably.

Seismicity rates are nearly constant on long temporal and spatial scales at tectonic plate boundaries. This stationarity is related to the steady-state motion of tectonic plates, which leads to temporally constant stressing and seismicity rates. In contrast, on the fault scale, a quasi-periodic recurrence of characteristic events is expected from the classical elastic rebound theory (Reid, 1911). Although observed at some fault segments such as Nankai Trough (Hyodo et al., 2016), such quasi-periodic recurrences of mainshocks have not yet been convincingly documented at plate boundaries in general (Kagan & Jackson, 1991, 1995; Roth et al., 2017).

On short time scales, earthquake clustering is the most obvious seismicity pattern. Almost every large earthquake is immediately followed by a sequence of smaller magnitude events, so-called aftershocks, clustered around the mainshock rupture. The aftershock rate usually follows the empirical Omori-Utsu relation (Utsu, 1961),

© 2022. The Authors.

This is an open access article under the terms of the [Creative Commons Attribution License](https://creativecommons.org/licenses/by/4.0/), which permits use, distribution and reproduction in any medium, provided the original work is properly cited.

$$R(t) = K(c + t)^{-p} \quad (1)$$

where  $c$  describes the delay of the onset of the aftershock decay with the exponent  $p$ . The parameter  $c$  is typically in the order of minutes to days, and  $p$  scatters around 1. While earthquakes trigger aftershocks overall, they can suppress ongoing activity at some locations, which is explained by the so-called stress-shadowing effect, as, for example, recently shown for the 2019 Ridgecrest sequence (Marsan & Ross, 2021).

Furthermore, aseismic processes are also well-known to trigger time-dependent seismicity. This obviously concerns transient processes at volcanoes (Heimisson et al., 2015; Passarelli et al., 2013), aseismic slip on faults as afterslip (Perfettini & Avouac, 2004) or slow slip events (Lohman & McGuire, 2007; Segou & Parsons, 2020), or anthropogenically triggered seismicity related to subsurface use (Becker et al., 2010; Grigoli et al., 2018).

Whether empirical or physical, any seismicity model must be able to reproduce the observed statistical characteristics of time-dependent seismicity. Well-known statistical models have been established to reproduce short-term aftershock triggering or mainshock recurrences. The epidemic type aftershock sequence (ETAS) model (Ogata, 1988) is widely used to reproduce earthquake clustering. On the other hand, for example, the Brownian Passage Time model (Matthews et al., 2002) and the stress release model (Vere-Jones, 1978) are used for simulations of quasi-periodic recurrences of mainshocks at the same fault. Those statistical models can successfully describe either aftershock patterns or seismic cycles and stress-shadowing effects but fail to model both. In contrast, seismicity models considering explicitly the real stress changes can do it. Those physics-based seismicity models are additionally an indispensable prerequisite for understanding earthquake triggering and can make predictions of time-dependent earthquake rates outside the range of previous observations. Among the class of physics-based seismicity models, two models are widely used to study seismicity patterns: (a) the Coulomb Failure (CF) model, and (b) the rate-state (RS) model based on a laboratory-derived constitutive RS dependent friction law (Dieterich, 1994). Both models were developed for shear cracks and use time-dependent stress changes as input (in a Coulomb stress approximation).

The CF model assumes instantaneous earthquake triggering when the absolute Coulomb stress exceeds a static strength threshold. The predicted earthquake rate correlates linearly with the stressing rate if a pre-existing population of potential faults with uniformly distributed stress is assumed, as long as stress increases. In contrast, a complete absence of seismicity is expected during periods of stress shadows after stress drops. Because a retarded triggering of earthquakes is not considered, the CF model cannot explain aftershocks solely by the coseismic stress changes of the mainshock. It requires the involvement of secondary stress changes to reproduce the characteristics of aftershock sequences, such as delayed stress changes due to (a) poroelastic response (Nur & Booker, 1972), (b) pore-pressure diffusion (Miller et al., 2004), or triggered postseismic slip, the so-called afterslip (Perfettini & Avouac, 2004).

The RS model posited by Dieterich (1994) is based on the assumption that fault slip is described by a specific constitutive RS dependent friction law derived from laboratory experiments. It assumes that frictional instabilities occur in a population of fault patches in a way that the earthquake rate is initially constant for constant tectonic stressing. In contrast to CF, it depends only on the stress change and not on the absolute stresses. RS explains, like CF, a constant earthquake rate for constant stressing and a rate decrease during periods of stress shadows. Additionally, it reproduces an Omori-Utsu type aftershock decay following a positive stress step. While the CF model has additional to the stress loading and threshold only one model parameter, the RSM has three model parameters. Its derivation is quite complex and uses several additional intrinsic assumptions. In a recent study, Heimisson and Segall (2018) revisited the RS theory with a different assessment and interpretation of the various model assumptions.

The new effective media model developed in this study is a modified CF model, which accounts for delayed nucleation of both tensile and shear cracks, simply by a stress-dependent mean time-to-failure. We first introduce the concept of the effective media approach and the modified CF model, derive the theoretical implications, and then discuss the model predictions in context with some field observations for induced seismicity, aftershock decays, and stress shadow effects in comparison to the established CF and RS models.

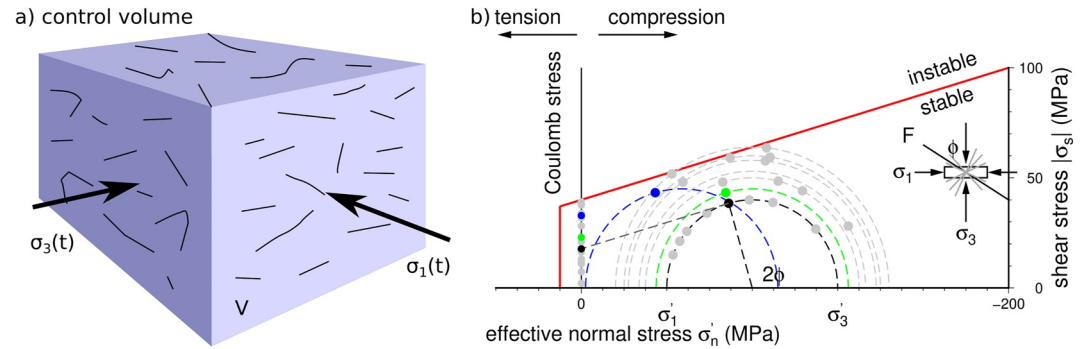


**Figure 1.** Conceptual sketch to derive an effective media approach for the distribution of faults or asperities sources in an effective media approach. (a) An infinite number of sources of different length and orientation are randomly distributed in a rock volume  $V$ . As some of them have experienced slip, and others not yet, the stress field in the rock volume is heterogeneous. (b) The Coulomb Failure line is plotted in a Mohr stress diagram, where colored circles indicate the state of stress on individual faults. The heterogeneous stress in  $V$  was replaced by a substitute media with an effective, homogeneous stress. Each source is considered independently in the center of the rock volume with its orientation conserved. The Coulomb stress of each source,  $\sigma_c$ , aligns on the Coulomb stress axis. If the rock volume is externally loaded (dashed Mohr circles), the same stress change is assumed to apply to all sources in  $V$  and the  $\sigma_c$  is uniformly shifted on the Coulomb stress axis.

## 2. Time-Dependent Stress Response Model (TDSR)

### 2.1. Concept

The earthquake rate is the number of events in a given volume and time interval with magnitudes above a completeness value  $M_c$ . We define an elementary rock volume  $V$  that undergoes a uniform time-dependent change in stress or pressure. The volume is cut through by pre-existing faults and fractures, which may possibly support an earthquake rupture (Figure 1a for illustration). The faults or neighboring rock contains local stress peaks ("sources") of uneven areas of varying size, which may be viewed as asperities. In the effective medium approach, the interaction of the sources is considered by replacing the rock volume with a substitute medium with average properties (effective modules) depending on the fault density (Dahm & Becker, 1998). The distribution of average background stress (represented by principal effective stresses  $\sigma'_1$  and  $\sigma'_3$ ) and Coulomb stresses at the individual sources can be visualized in a Mohr Coulomb diagram (Figure 1b). Although the absolute stress at each source within  $V$  can vary and also be different from the ambient background stress, the change in Coulomb stress is assumed to be equal. For instance, the Coulomb stress changes  $\Delta\sigma$  may occur by a redistribution of stress in  $V$  after a major earthquake, by other types of internal aseismic dislocation sources beside  $V$  or by pore pressure changes in the rock volume itself.

In the CF model, an earthquake is instantaneously triggered when the Coulomb stress  $\sigma_c$  at the source exceeds the inherent cohesive strength  $S_0$  (Figure 2). For a constant and uniform stressing rate  $\dot{\sigma}_c$ , the time-to-failure  $t_f$  for a source is in this case simply given by  $t_f = \zeta / \dot{\sigma}_c$  with  $\zeta = S_0 - \sigma_c$  being the difference between strength threshold and the actual Coulomb stress at the source. Thus, a constant rate  $r_0$  results in the CF model for a uniform pre-stress density distribution  $\chi(\zeta) = (r_0 / \dot{\sigma}_c) H(\zeta)$ , where  $H$  is the Heaviside function ( $H(x) = 1$  for  $x \geq 0$  and 0 else).

While the deterministic failure criterion of the CF model is simple and thus attractive, it is an oversimplification. Instead of a fixed threshold and instantaneous triggering, instabilities are realistically expected to occur at various stress levels with stress-dependent nucleation times for instabilities to grow into seismic ruptures. Based on experimental data on stress corrosion of rocks (Innocente et al., 2021) and subcritical crack growth, the mean time-to-failure  $\bar{t}_f$  is an exponential function according to

$$\bar{t}_f = t_0 e^{\frac{\zeta}{\delta\sigma}} \quad (2)$$

The constant  $t_0$  is the mean delay time for a critically stressed source ( $\zeta = 0$ ) and can be assumed very small. The parameter  $\delta\sigma$  controls the increase of  $\bar{t}_f$  with  $\zeta$  and is in our study denoted as skin parameter (see Figure 2b). In the limit of  $\delta\sigma \rightarrow 0$ , the time-to-failure becomes  $\infty$  for  $\zeta > 0$  (stable) and 0 for  $\zeta < 0$  (instantaneous failure); thus leading to the CF model.

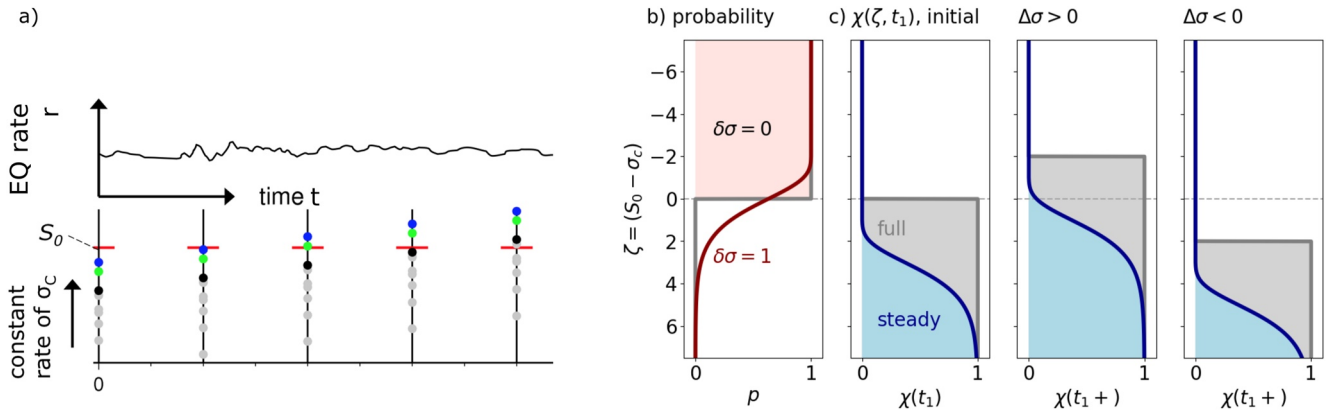


**Figure 2.** Schematic sketch to describe the implementation of time dependent stress loading and earthquake triggering. (a) The distribution of  $\sigma_c^{(k)}$  on the Coulomb stress axis in Figure 1b is plotted as a function of time assuming a uniform increase of stress stages at each asperity. A constant earthquake rate  $r$  is indicated. (b) Trigger probability function  $p(\zeta)$ . The Coulomb Failure (CF) model assumes a step function trigger probability  $p = H(\sigma - S_0) = H(-\zeta)$  (gray line, associated with  $\delta\sigma = 0$ ). In the TDSR model, the probability is a smooth function due to a non-zero skin parameter  $\delta\sigma$  (red line). (c) Normalized distribution of source stresses are defined by an initial susceptibility function  $\chi(\zeta, t_1)$ . The initial distributions at time  $t_1$  for  $\delta\sigma = 0$  are assumed uniform at  $\zeta > 0$  (greyish area, CF model). For  $\delta\sigma > 0$  the equilibrium distribution is a smooth function (bluish area). Due to stress loading or unloading, the distributions are shifted either to higher or lower levels on the stress axis with time.

The exponential law has been suggested for both quasi-static crack propagation of tensile (Aktinson, 1984) and shear cracks in brittle rock (Ohnaka, 2013) if  $\zeta$  is either interpreted as a function of the stress intensity factor or the difference between strength and Coulomb stress, respectively. For instance, Scholz (1968) used the exponential form of  $1/\bar{t}_f$  to explain the mechanism of creep in brittle rock. The same law has been used to explain crack growth in ceramics (Wiederhorn et al., 1980) or the number of acoustic emissions under creep (e.g., Ohnaka (1983) and references therein). We follow Scholz (1968) and Ohnaka (2013) and define  $\zeta$  by  $S_0 - \sigma_c$ . However, the concept can be applied equally well to tensile crack seismicity or other forms of the mean decay times.

Given the mean time-to-failure  $\bar{t}_f$ , the mean failure rate for  $N$  sources is given by  $N/\bar{t}_f$ . Thus, the distribution of sources at the different stress levels has to be considered to calculate the total event rate of the volume. This time-dependent density distribution of sources is defined by  $\chi = \chi(\zeta, t)$  and the total rate at time  $t$  becomes

$$R(t) = \int_{-\infty}^{\infty} \frac{\chi(\zeta, t)}{\bar{t}_f(\zeta)} d\zeta, \quad (3)$$

where  $\bar{t}_f(\zeta)$  is given by Equation 2 and independent of time. In order to use this relation for rate forecasts, the evolution of  $\chi(\zeta, t)$  is needed. To solve it analytically or numerically, we use the following assumptions and simplifications:

1. Each source in  $V$  is loaded by the same stress and acts independently (effective media approach).
2. In addition to external loading, each source is subject to static fatigue described by Equation 2.
3. Each source fails only once during a simulation, that is, the stress drop  $\Delta S$  is significantly larger than the loading stress during the simulation, and failed sources can be removed from the distribution of available sources.
4. For simplifying the following analytical calculations, we ignore that  $\zeta$  is limited by the maximum value  $S_0$ . This assumption holds for  $\delta\sigma \ll \Delta S$ .

## 2.2. Analytic Solutions

The model forecasts can be analytically derived for some simplified stress scenarios. These solution can be all derived from the total time derivative of  $\chi$  being equal to the negative event rate, namely

$$\frac{d\chi(\zeta, t)}{dt} = \frac{\delta\chi(\zeta, t)}{\delta t} + \frac{\delta\chi(\zeta, t)}{\delta\zeta} \frac{d\zeta}{dt} = -\chi(\zeta, t) / \bar{t}_f(\zeta). \quad (4)$$

The detailed derivations of the following solutions can be found in Appendix A.

### 2.2.1. Uniform Initial Distribution With Constant Loading

For the case of an initially uniform stress distribution for  $\zeta > \zeta_{\min}$  at  $t = 0$ , that is,  $\chi(\zeta, 0) = \chi_0 H(\zeta - \zeta_{\min})$  (gray line in Figure 2c) and a constant stressing rate  $\dot{\sigma}_c$  for times  $t > 0$ , the time-dependent seismicity rate is

$$R(t) = \chi_0 \dot{\sigma}_c \frac{1 - e^{-\frac{\dot{\sigma}_c}{t_0 \dot{\sigma}_c} \left(1 - e^{-\frac{\dot{\sigma}_c t}{\dot{\sigma}_c}}\right) e^{-\frac{\zeta_{\min} - \dot{\sigma}_c t}{\dot{\sigma}_c}}}}{1 - e^{-\frac{\dot{\sigma}_c t}{\dot{\sigma}_c}}}. \quad (5)$$

The solution can be compared to the rate expected in the CF and RS model. In the CF model,  $R(t) = \chi_0 \dot{\sigma}_c H(t - \zeta_{\min}/\dot{\sigma}_c)$ , that is, the CF model, unlike ours, predicts a sudden onset of a constant seismicity rate at time  $t = \zeta_{\min}/\dot{\sigma}_c$ . In contrast, the original RS model of Dieterich (1994) always assumes a stationary background seismicity ( $r \equiv r_0$ ) as starting condition and thus cannot deal with a subcritical initial stress state. Heimissson et al. (2022) extended the RS-framework for subcritical initial stress states (RS<sub>subcrit</sub>). The solution of their Equation 1 for  $\Delta S_c = \zeta_{\min}$  and a constant stressing rate  $\dot{\sigma}_c$  yields  $R(t) = r_0 H(t - \zeta_{\min}/\dot{\sigma}_c)$ , that is, an instantaneous onset of a constant rate at  $t = \zeta_{\min}/\dot{\sigma}_c$  as the CF model.

### 2.2.2. Stationary Seismicity

The stress distribution associated to a constant seismicity rate  $R(t) = r_0$  for a given stressing rate  $\dot{\sigma}_c$  is given by (blue line in Figure 2c)

$$\chi_s(\zeta) = \frac{r_0}{\dot{\sigma}_c} \exp\left(-\frac{\dot{\sigma}_c}{t_0 \dot{\sigma}_c} e^{-\frac{\zeta}{\dot{\sigma}_c}}\right). \quad (6)$$

Here, the subscript in  $\chi_s$  is used to denote that this distribution is stationary, that is, time-independent. The prefactor  $\chi_0 = r_0/\dot{\sigma}_c$  expresses the susceptibility of the rock volume.

### 2.2.3. Stress Step

Here it is assumed that the initial pre-stress distribution is given by  $\chi_s$  related to constant stressing and seismicity rate,  $\dot{\sigma}_c$  and  $r_0$ , respectively. A stress step  $\Delta\sigma_c$  is applied at time  $t = 0$  followed by a loading with constant stressing rate  $\dot{\sigma}_{c,a}$  at  $t > 0$ . The seismicity rate is in this case given by

$$R(t) = \frac{r_0 \frac{\dot{\sigma}_{c,a}}{\dot{\sigma}_c}}{\left(\frac{\dot{\sigma}_{c,a}}{\dot{\sigma}_c} e^{-\frac{\Delta\sigma_c}{\dot{\sigma}_c}} - 1\right) e^{-\frac{\dot{\sigma}_{c,a} t}{\dot{\sigma}_c}} + 1} \quad \text{for } \dot{\sigma}_{c,a} \neq 0 \quad (7)$$

and

$$R(t) = \frac{r_0}{e^{-\frac{\Delta\sigma_c}{\dot{\sigma}_c}} + \frac{\dot{\sigma}_c}{\dot{\sigma}_{c,a}} t} \quad \text{for } \dot{\sigma}_{c,a} = 0. \quad (8)$$

For positive stress steps, the second equation is identical to the Omori-Utsu law Equation 1 with  $p = 1$ ,  $c = \frac{\dot{\sigma}_c}{\dot{\sigma}_{c,a}} \exp\left(-\frac{\Delta\sigma_c}{\dot{\sigma}_c}\right)$ , and  $K = \frac{r_0 \dot{\sigma}_c}{\dot{\sigma}_{c,a}}$ . While the CF model cannot predict Omori-type aftershocks, both equations are identical to the solutions of the RS-model for the same conditions, namely, Eq. (12) and (13) of Dieterich (1994) with  $A\sigma \equiv \delta\sigma$ ,  $r \equiv r_0$ ,  $\dot{\tau}_r \equiv \dot{\sigma}_c$ , and  $\dot{\tau} \equiv \dot{\sigma}_{c,a}$ .

### 2.2.4. Changing Stressing Rates

The solution for a changing stressing rate from  $\dot{\sigma}_c$  for  $t \leq 0$  to the new constant stressing rate  $\dot{\sigma}_{c,a}$  for  $t > 0$  can be directly derived from Equation 7 by setting  $\Delta\sigma_c = 0$ , yielding

$$R(t) = \frac{r_0}{\left(1 - \frac{\dot{\sigma}_c}{\dot{\sigma}_{c,a}}\right) e^{-\frac{\dot{\sigma}_{c,a} t_b}{\dot{\sigma}_c}} + \frac{\dot{\sigma}_c}{\dot{\sigma}_{c,a}}}. \quad (9)$$

A ramp-like excitation in stress, or a box-car stressing rate with duration  $t_b$  and  $\dot{\sigma}_c$  for  $t < 0$  and  $t > t_b$  and  $\dot{\sigma}_{c,a}$  elsewhere, can be constructed from Equation 9 by

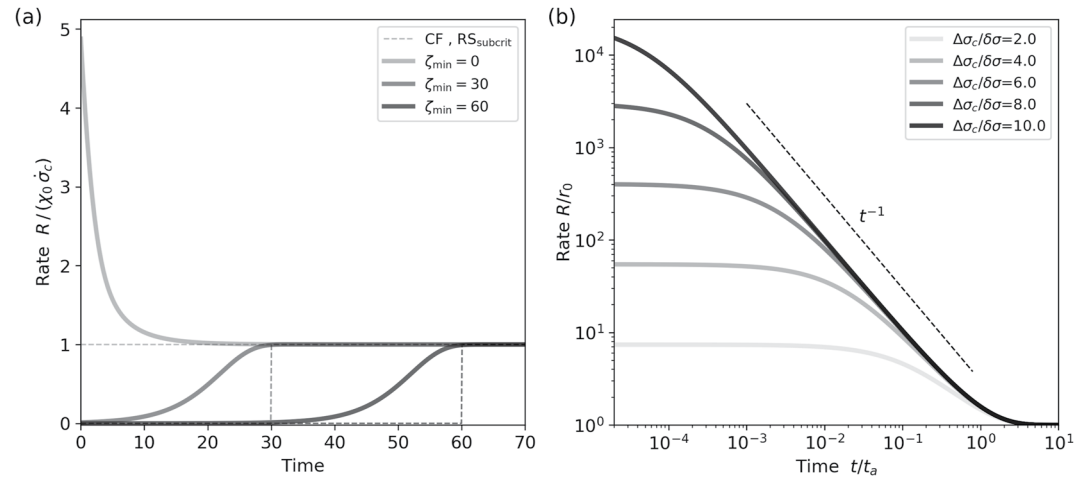


**Figure 3.** (a) Seismicity expected after the onset of a constant stressing rate  $\dot{\sigma}_c$  at time 0 for a uniform pre-stress distribution  $\chi(\zeta) = \chi_0 H(\zeta - \zeta_{\min})$ . The curves refer to simulations which match Equation 5. The model parameters are  $\dot{\sigma}_c = t_0 = 1$  and  $\delta\sigma = 5$ . For comparison, the dashed lines show the correspondent (identical) forecasts of Coulomb Failure (CF) and rate-state (RS<sub>subcrit</sub>). (b) Relative seismicity rate increase  $R/r_0$  following positive stress steps as a function of time in units of  $t_a \equiv \delta\sigma/\dot{\sigma}_c$ . Note that the curve shape only depends on  $\Delta\sigma_c/\delta\sigma$ . The lines refer to numerical simulations which match Equation 7. For times  $t \ll t_a$ , the result is described by the Omori law (dashed curves) with  $p = 1$  (dashed line) with  $K$  and  $c$ -values depending on the stress step according to Equation 8.

$$R(t) = R_1([0 : t_b]) + R_2([t_i : \infty] - t_b), \quad (10)$$

where  $t_i = -\frac{\delta\sigma}{\dot{\sigma}_c} \ln\left(1 - e^{-\frac{\sigma_{c,a} t}{\delta\sigma}}\right)$  and  $R_1$  given by Equation 9 and  $R_2$  by Equation 9 with interchanging  $\dot{\sigma}_c$  and  $\dot{\sigma}_{c,a}$ .

### 3. Applications

While the analytic solutions (Equations 5–10) can be used for simple stressing histories, the integral in Equation 3 must be solved numerically for more complex cases. The numerical model implementation is straightforward, and the structure of the simple algorithm, which we used for the simulations presented in this work, is provided in Appendix A2.

#### 3.1. Synthetic Examples

The following synthetic case studies are used to illustrate the response to some generic setups.

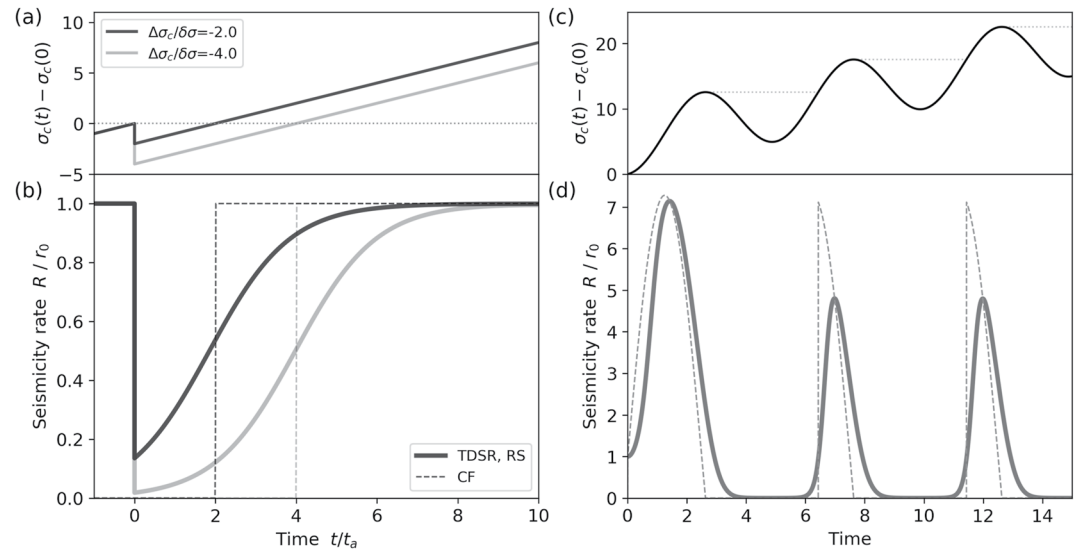
##### 3.1.1. Subcritical Uniform Pre-Stress Distribution

Figure 3a shows the TDSR forecasts for the case of a uniform pre-stress distribution and constant loading  $\dot{\sigma}_c$ . The numerical simulations of the TDSR model exactly resemble Equation 5. The three analyzed  $\zeta_{\min}$  values of 0, 3, and 6 lead to different responses. For  $\zeta_{\min} = 0$ , the rate decays with time until it reaches the stationary seismicity rate  $r_\infty = \chi_0 \dot{\sigma}_c$ . In contrast, the seismicity rate is initially much lower than  $r_\infty$  and only starts to accelerate and converge with some delay for  $\zeta_{\min} > 0$ . In comparison to the predictions of CF and RS<sub>subcrit</sub>, which are both identical for this setup, the onset of the seismicity is smooth and occurs earlier. The accelerated seismicity already reached the steady-state when the other models predicted the sudden onset. Thus, for a fixed onset time of the seismicity, the estimated  $\zeta_{\min}$  value for TDSR will be larger than for CF and RS<sub>subcrit</sub> (e.g., see the application to Groningen in Section 3.2.1).

##### 3.1.2. Aftershock Triggering

The TDSR model with stationary pre-stress distribution (Equation 6) leads to Omori-type aftershock sequences with  $p = 1$  for positive stress steps at  $t = 0$ . Figure 3b shows the immediate rate increase in a double logarithmic plot as a function of time after the stress step, where the stressing rate remains constant, that is,  $\dot{\sigma}_{c,a} = \dot{\sigma}_c$ . The numerical simulations exactly match Equation 7. It is important to note that (a) the aftershock rate is directly





**Figure 4.** Rate decrease in response to a stress drop at time  $t = 0$  (a). As for positive stress steps, the rate simulations in (b) are also described for negative stress steps (here,  $\Delta\sigma_c/\delta\sigma = -2$  and  $-4$ ) by Equation 7. (d) Seismicity response resulting from cyclic loading shown in (c) according to a cosine starting at time 0, where the model parameters are set to  $\dot{\sigma}_c = t_0 = \delta\sigma = 1$ . In all time-dependent stress response simulations, an initially constant seismicity rate and a constant background stressing rate is assumed. While the rate-and-state model predicts the same response in all cases, the Coulomb Failure model (dashed lines) predicts a total quiescence of length  $t_a |\Delta\sigma_c|/\delta\sigma$  after the stress drop in (a and b) and during stress shadows (d) marked by horizontal lines in (c).

proportional to the background rate  $r_0$ , (b) the maximum seismicity rate at  $t = 0^+$  is  $r_0 \exp(\Delta\sigma_c/\delta\sigma)$ , (c) the duration of the aftershock decay is given by  $t_a \equiv \delta\sigma/\dot{\sigma}_c$ , and (d) the time delay until the onset of the  $1/t$  decay ( $c$ -value in Equation 1) depends on the stress step. The larger the step, the shorter the delay.

### 3.1.3. Stress Shadowing

The seismicity rate is commonly assumed to decrease during periods in which the absolute stress dropped below its previous maximum value (so-called stress shadows). This stress shadow effect is also known as Kaiser effect. To illustrate the response of the TDSR model to stress shadows, we run simulations with stationary pre-stress distributions. Figure 4a shows the result for sudden stress drops ( $\Delta\sigma_c < 0$ ), which are also described by Equation 7. For instance, a volume of rock on the rupture plane of a large earthquake may experience a co-seismic negative stress step when the rupture front has passed by. The TDSR model predicts identically to the RS model that the seismicity rate drops instantaneously in this case from  $r_0$  to  $r_0 \exp(\Delta\sigma_c/\delta\sigma)$  and then recovers slowly until it reaches the background level at approximately  $6 t_a$ . Thus, the memory for stress drops is a few times larger than for positive stress steps, that is, aftershock sequences. In contrast, the CF model (i.e., the TDSR model in the limit for  $\delta\sigma \rightarrow 0$ ) predicts an absolute quiescence of length  $t_a |\Delta\sigma_c|/\delta\sigma$  followed by an instantaneous recovery of the background rate. Similarly, for cyclic loading shown in Figure 4b, the TDSR model predicts smooth transitions from almost zero rates to high activity and vice versa, while CF shows sharp transitions.

### 3.1.4. Arbitrary Stressing Histories in Space and Time

In general, stress changes are complex in time, for example, due to multiple stress sources such as earthquakes, aseismic slip, or pore-pressure changes, and no analytical solution is known. In addition, the stress evolution is usually spatially inhomogeneous because distances to sources vary and physical properties such as fault density and orientation or stress state are spatially heterogeneous (Hardebeck, 2021). In this case, the model must be numerically solved by discretizing the stress evolution in space and time and applying the algorithm described in Appendix A2 independently for each spatial grid point.

It is important to note that TDSR leads to identical forecasts for any arbitrary stress history as RS if the initial condition is critical, a reasonable assumption for natural seismicity at plate boundaries if no other information is available. This congruency is expected given that (a) the response to stress steps (Equations 7 and 8) and changes in the stressing rate (Equation 9) is for both models identical, and (b) any stressing history can be well

approximated by stress steps and periods of constant stressing rates using sufficiently small time steps. However, for confirmation, we also performed simulations with complex stress histories consisting of multiple stress steps with variable stressing rates in between, finding identical forecasts of TDSR and RS.

### 3.2. Applications to Real Data

Analytic solutions and simple synthetic model runs are helpful to clarify and demonstrate general model properties, but the ultimate goal of any seismicity model is the application to real data. In the following, we briefly discuss some examples of TDSR applications to induced and natural seismicity, which are related to the synthetic case studies.

#### 3.2.1. Groningen

The Groningen field, Netherlands, is one of the largest gas reservoirs in the world. The gas production started in 1963, but the first earthquake related to gas extraction was only detected in 1991. At that time, the reservoir pore pressure dropped already approximately 10 MPa, related to a rock stress increase of similar magnitude, generally taken as evidence that before production, most Groningen faults were far from critical stress (Candela et al., 2018). Between 1991 and 2021, more than 350 earthquakes with magnitude  $M_L \geq 1.5$  have been recorded.

The occurrence of felt earthquakes accompanying the gas production initiated dense instrumentation, numerous field studies, and the development and application of many seismicity models for explaining and quantifying the observed seismicity, see the recent review of Kühn et al. (2022). For example, a CF model version was developed by Bourne and Oates (2017) and Bourne et al. (2018) assuming that the stresses at the activated faults are in the tail of the pre-stress distribution. The latter assumption was used to apply extreme value statistics to explain the observed non-linear response to the stress changes. Furthermore, different RS model implementations have been applied to Groningen, among others Dieterich's model (RS) by Richter et al. (2020) and the subcritical RS model (RS<sub>subcrit</sub>) by Heimisson et al. (2022). Recall that TDSR forecasts are identical to RS forecasts under the assumption of critical initial conditions. Thus, all Richter et al. (2020) results for RS can be interpreted as TDSR predictions with  $\delta\sigma = A\sigma$ ,  $r_0 \equiv r_0$ , and  $\dot{\sigma}_c \equiv A\sigma/t_a$  using Equation 6 as initial condition. Previous model applications were based on estimated stress changes in space and time, including available fault information. Here, we do not want to compete with those detailed studies but only want to demonstrate the potentials of the TDSR model to account for subcritical stress states and leave a detailed analysis to future work. For simplification, we only consider the annual changes of the mean pore pressure in the field and assume that Coulomb stress changes are proportional to the size of the pore pressure drop.

We compare the TDSR forecasts with the corresponding results of the CF, RS, and RS<sub>subcrit</sub> models. To reduce the number of free model parameters, we constrained the pre-factors by the condition that the total number of forecasted earthquakes equals the observed events in 1991–2021. With this constraint, CF considering continuous tectonic stressing has no free parameter, CF assuming a subcritical initial stress state (CF<sub>subcrit</sub>) has one ( $\zeta_{\min}$ ), RS has two ( $A\sigma$  and  $\dot{\sigma}_c$ ), and RS<sub>subcrit</sub> has three parameters ( $A\sigma$ ,  $\dot{\sigma}_c$ , and  $\zeta_{\min}$ ). For both models, CF<sub>subcrit</sub> and RS<sub>subcrit</sub>, the stress gap had to be equalized by the gas production at the time when the seismic activity started; thus, we set  $\zeta_{\min} = 8.5$  MPa, which was equalized by the induced stress increase just before the first observed earthquakes in 1991. Furthermore, we set  $A\sigma = 1$  MPa which is in the range of the results of Richter et al. (2020). The free parameters of the TDSR model depend on the assumed initial conditions. Assuming a constant background seismicity, that is, a stationary TDSR pre-stress distribution according to Equation 6, leads to forecasts which are independent of  $t_0$  and identical to the RS model for  $\delta\sigma = A\sigma$  using the same stressing rate  $\dot{\sigma}_c$ . However, the TDSR model also works for subcritical stress conditions with zero background stressing. Instead of  $\dot{\sigma}_c$ , the model depends on  $t_0$  and the parameters required to characterize the pre-stress condition; for example,  $\zeta_{\min}$  for a uniform pre-stress distribution, or the mean  $\bar{\zeta}$  and standard deviation  $\zeta_\sigma$  for a Gaussian distribution.

Figure 5b shows the results of the TDSR model in comparison to the other models, where we set the remaining free parameters in order to fit the observed annual rates of earthquakes with magnitudes larger than 1.45, that is, the estimated completeness magnitude since 1993 (Dost et al., 2017; Heimisson et al., 2022). We find that

1. The CF model with uniform pre-stress conditions cannot fit the observations, neither for critical nor for subcritical conditions.



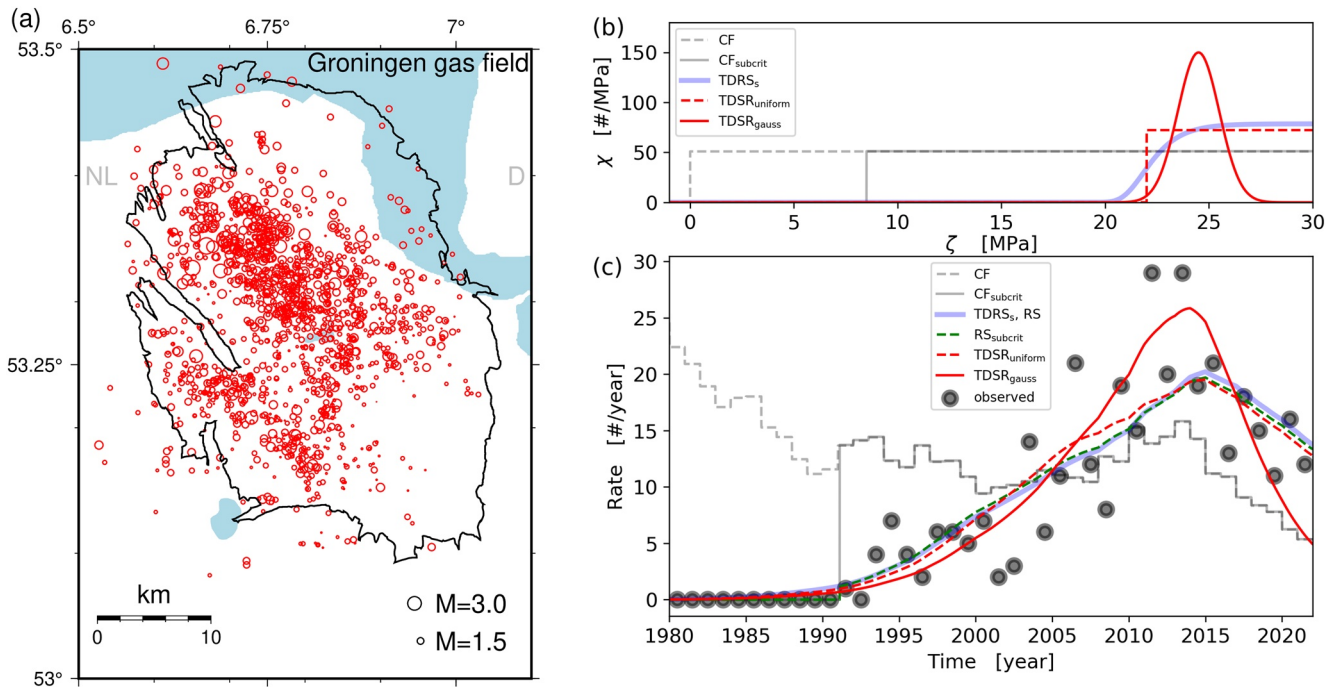


**Figure 5.** Application of the time-dependent stress response (TDSR) model to the Groningen gas field (see Figure 6b for its location within Europe). (a) shows the gas field contour (black line) with recorded earthquakes (circles). (b) Assumed alternative pre-stress distributions: (i) stationary initial conditions ( $TDSR_s$ ) corresponding to a background stressing rate of  $\dot{\sigma}_c = 3.3$  Pa/year, (ii) a uniform stress distribution of the sources for  $\zeta > 22$  MPa ( $TDSR_{uniform}$ ), and (iii) a Gaussian distribution with a mean of 24.5 MPa and a standard deviation of 1 MPa ( $TDSR_{gauss}$ ). (c) The resulting seismicity response of the TDSR model to the mean pressure changes in the Groningen gas field, using  $t_0 = 10^{-4}$  years and  $\delta\sigma = 1$  MPa. Here, points refer to the annual rate of observed earthquakes with magnitudes larger than 1.45, that is, the estimated completeness magnitude since 1993 (Dost et al., 2017; Heimissson et al., 2022). The largest earthquake occurred 2012 with a magnitude 3.6. For comparison, the corresponding curves are shown for the subcritical Coulomb Failure (CF) model ( $CF_{subcrit}$ ) and the subcritical rate-and-state (RS) model of Heimissson et al. (2022) ( $RS_{subcrit}$ ). In both cases, an initial stress gap was set to 8.5 MPa, reached just before the first observed earthquakes in 1991. In addition, a background stressing rate of  $\dot{\sigma}_c = 17$  kPa/year is assumed in  $RS_{subcrit}$ . Note that the RS model of Dieterich (1994) leads to an identical forecast as  $TDSR_s$ .

2. TDSR and RS assuming an initially constant background seismicity rate lead to identical fits. For a reasonable data fit, the background stressing rate must be extremely low ( $\dot{\sigma}_c = 3.3$  Pa/year in Figure 5).
3.  $RS_{subcrit}$  leads to almost the same result as RS but with a significantly larger background stressing rate, namely 17 kPa/year for the same  $A\sigma$  value.
4. To get similar fits, the pre-stress conditions in the TDSR model depend on  $t_0$ ; the shorter  $t_0$ , the larger the pre-stress gaps, or vice versa. For a mean nucleation time at critical stress of  $t_0 = 10^{-4}$  years ( $\approx 53$  min), the stress gap is significantly larger ( $\zeta_{min} = 22$  MPa, respectively  $\bar{\zeta} = 24.5$  MPa) compared to 8.5 MPa estimated by  $CF_{subcrit}$  and  $RS_{subcrit}$ .
5. The shape of the ongoing seismicity rate decay depends strongly on the assumed pre-stress distribution shown in Figure 5a. While the predictions of the RS models and the TDSR model either with background stressing or uniform pre-stress distribution behave similarly, the decay is much steeper if a Gaussian distribution of sources is assumed. In the latter case, the depletion of available sources starts to dominate the activity at presence and is expected to lead to a rapid disappearance of the activity in the near future. Because this could have important implications for seismic hazard studies, a more detailed analysis is needed using more specific stress calculations in space and time and an estimate of the initial stress distribution considering the regional stress field and fault orientations. Such a comprehensive analysis is beyond the scope of this study and is the subject of future work.

### 3.2.2. Fits to Aftershock Sequences

Important applications of seismicity models are forecasts of aftershock sequences because aftershocks are sometimes very destructive and deadly. Major aftershock sequences are typically observed at tectonic plate boundaries, where a constant background stressing rate can be assumed for loading the fault system. Thus, in the absence of

any additional information, a constant background rate as initial condition is reasonable in this case. Then, as discussed before, the TDSR model forecasts are identical to the RS model with  $\delta\sigma = A\sigma$ .

Thus, the detailed existing studies and comparative tests for the RS model can be exploited in terms of the TDSR model. Those model studies made use of detailed slip models for the mainshocks and large secondary stress changes to estimate the seismicity rate changes in space and time; among others, for the 1992 M7.2 Landers sequence (Hainzl et al., 2009), 2004 M6 Parkfield and the 2011 M9 Tohoku sequences (Cattania et al., 2014), the 2010–2012 Canterbury sequence (Cattania et al., 2018), and the 2016–2017 Central Italy earthquake cascade (Mancini et al., 2019). Those model applications provided, in general, good data fits. Furthermore, pseudo-prospective forecast experiments were conducted for several sequences using the consistency and comparative tests introduced by CSEP (Collaboratory for the Study of Earthquake Predictability, <https://csepe-esting.org>). The comparison of the TDSR/RS forecasts with those of the purely empirical ETAS model showed that the physics-based models partly outperform the empirical ones (Cattania et al., 2018; Mancini et al., 2019; Woessner et al., 2011). These studies for aftershock sequences also provide estimates of  $A\sigma$ , that is,  $\delta\sigma$ , in the range of 0.01–0.1 MPa.

As mentioned in Sections 2.2.3 and 3.1.2, TDSR predicts that the duration  $t_a$  of the aftershock decay is given by  $t_a = \delta\sigma/\dot{\sigma}_c$ . Thus, it is inversely related to the tectonic (background) stressing rate  $\dot{\sigma}_c$ , implying that aftershock sequences in intraplate regions last longer. For a stress drop of 1 MPa, assuming a reloading time of 100 and 1,000 years corresponds to stressing rates of 0.01 and 0.001 MPa/year, respectively, which would result in  $t_a$  in the range of 1–10 years and 10–100 years, respectively, using the estimated range of  $\delta\sigma$  values. These values are consistent with empirical observations, for example, the results of Hainzl and Christophersen (2017) for empirical fits to more than 300 recorded earthquake sequences, which yielded a mean value of about 30 years, but with a large proportion of significantly shorter  $t_a$ -values.

Another prediction of the TDSR model is that the time delay until the onset of the  $1/t$  decay ( $c$  value) depends on the size of the stress step. The larger the step, the shorter the delay, according to  $c = t_a \exp(-\Delta\sigma_c/\delta\sigma)$ . Therefore, the onset of aftershock decay near the rupture should be quicker than for aftershocks in the far-field. For example, assume  $t_a$  in the range of 1–100 years and the mean value  $\delta\sigma = 0.05$  MPa. Then, a stress change of 1 MPa results in  $c$  values between 0.06 and 6 s, while a stress change of 0.1 MPa results in  $c$  values between 50 days and 13.5 years. This example shows that the predicted difference is enormous and could have far reaching implications. In practice, however, the test is difficult. First, short  $c$  values cannot be detected due to the incompleteness of earthquake catalogs in the first hours to days after a mainshock when small earthquakes cannot be recorded because of overlapping waveforms (Hainzl, 2016). Second, longer  $c$  values are masked by secondary aftershock triggering. More distant aftershocks are often triggered by closer, early aftershocks rather than the more distant mainshock. Therefore, analyzing and testing the predicted stress dependence of the  $c$  value requires careful consideration.

Finally, TDSR predicts that the response to stress steps is proportional to the background rate  $r_0$  (Equations 7 and 8 and Figure 3b). This prediction is in contrast to the empirical ETAS model, where the aftershock productivity is assumed to be independent of the background rate. Thus, TDSR predicts no aftershocks in ductile regions deforming aseismically and low aftershock productivity in regions of low seismic coupling. The latter agrees with the observation of Hainzl et al. (2019) that aftershock productivity is proportional to the seismic coupling derived from geodetic inversions in the Northern Chile subduction zone.

As seen by Figures 3b and 4a, TDSR predicts an Omori decay for positive stress steps and quiescence for stress drops. A combination of both is predicted for stress distributions with a negative mean value but a tail including positive values. Helmstetter and Shaw (2006) and Marsan (2006) theoretically showed that the aftershock decay in this case transitions to a quiescent phase after a short time. Such a distribution of stress steps is expected near the mainshock rupture, where stress drops on average but small-scale heterogeneities with positive stress changes exist. The prediction is consistent with observations for megathrust earthquakes, as recently shown by Toda and Stein (2022).

In general, mainshocks may also affect subcritically stressed regions. TDSR forecasts assuming subcritical prestress conditions differ from forecasts of the standard RS model and its subcritical version. While the response depends on the details of the prestress distribution, we explored a simplified setup to analyze the general effect. We compared the response to a stress step of  $\Delta\sigma/\delta\sigma = 10$  assuming critical initial conditions (uppermost curve

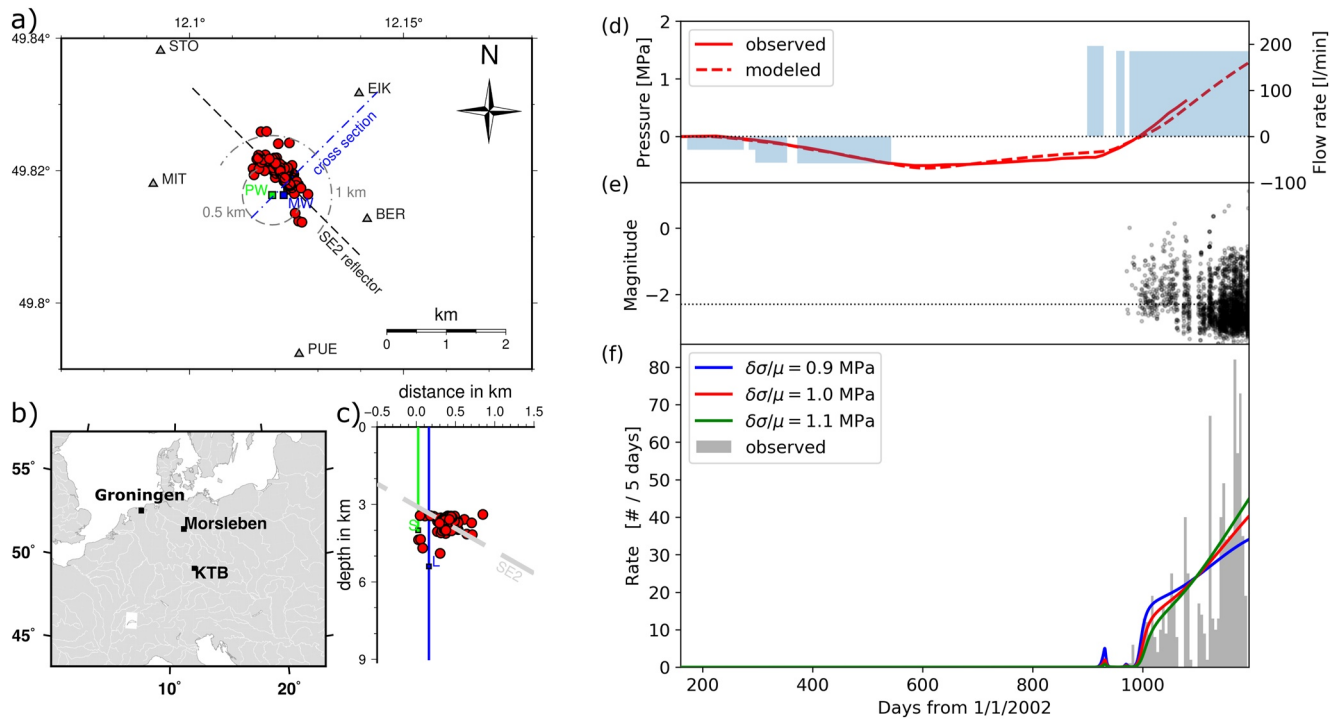


**Figure 6.** Longterm cyclic fluid production and injection experiment in crystalline rock at ~4,000 m depth in the pilot hole of the German Continental Deep drilling site. (a) Map view of the pilot (PW) and main well (MW), together with epicenters of earthquakes (red circles,  $-1.8 \leq M_L \leq 1$ ) induced during the injection phase (Shapiro et al., 2006). (b) Overview map and (c) cross-section along the profile indicated in (a). (d) Shows the injection rates (filled boxes), and measured (solid red) and predicted (dashed red) pore pressure at a depth of open section of the main well. (e) Occurrence of induced earthquakes and their magnitudes (taken from [Haney et al., 2011]). The dashed horizontal line indicates the selected magnitude of completeness,  $M_c = -2.3$ . (f) The observed earthquake rate ( $m \geq -2.3$ ) is compared to time-dependent stress response predictions for  $\dot{\sigma}_c = 30$  Pa/year and different values of  $\delta\sigma/\mu$ .

in Figure 3b) with the aftershock activity for subcritical prestress distributions where the initial values of  $\chi_s$  in Equation 6 are set to zero for  $\zeta < \zeta_{\min}$ . We find that values of  $\zeta_{\min}/\delta\sigma$  between 0 and 8 resemble the curves in Figure 3b related to reduced stress steps  $\Delta\sigma/\delta\sigma$  varying between 8 and 2. Thus, for increased subcriticality ( $\zeta_{\min}/\delta\sigma$ ), the aftershock productivity reduces, and the  $c$ -value increases. This effect could explain the low aftershock productivity (high Bath's law value) observed in stable intraplate regions (Page et al., 2016), where subcritical stress conditions are generally expected.

### 3.2.3. Examples of Stress Shadows Effects

Induced earthquakes are well suited as case studies for stress shadows when they are associated with a controlled, short-term variations in Coulomb stress, for instance related to periodic fluid injections in basement rocks or cyclic thermal loading of a mine gallery.

#### 3.2.3.1. KTB Experiment

The first example treats a sequential fluid production and injection experiment in 4 km depth at the German Continental Deep Drilling site (KTB) in Windischeschenbach, Bavaria, Germany (Figure 6). The KTB consists of two accessible boreholes drilled 200 m from each other into crystalline rock, the 4,000 m deep pilot well and the 9,100 m deep main well (Kümpel et al., 2006). Two distinct fault systems cut through the hydraulically connected wells. The hydraulic experiment started in June 2002 with a one-year production of 22,300 m<sup>3</sup> of saline water of 120°C from the open section of the pilot well between 3,850 m and 4,000 m depth (Kümpel et al., 2006). The drawdown of the fluid level in the pilot well reached 605 m at the end of the production phase in June 2003. The fluid level in the main well gradually dropped from zero to 50 m below the surface during the production phase, indicating a hydraulic connection between the two wells likely originating at a leakage in the casing of the main well between 5,200 and 5,600 m depth (Grässle et al., 2006). In June 2004, after a one-year recovery phase following the production, an injection experiment was conducted until April 2005. Overall, 84,500 m<sup>3</sup> of fresh-water, about four times the produced volume, was re-injected during 10 months in the same open-hole section

of the pilot hole. Although the injection rate was more or less constant between 185 and 196 l/min, the wellhead pressure varied between 9 and 12 MPa (Kümpel et al., 2006). In October 2004, 114 days after the start of the injection, the main hole became artesian with a rate of  $\sim 6.9 \times 10^{-4} \text{ m}^3/\text{min}$  ( $\sim 1 \text{ m}^3/\text{day}$ ) (Kümpel et al., 2006). Because of the hydraulic connection between the two wells, the water level in the main well directly measured the time-dependent pressure change  $\Delta P_f$  at the leakage point at a depth of  $\sim 5,500 \text{ m}$ . Using this and other information on the local hydraulic structure, Grässle et al. (2006) modeled the pressure field between the two wells using a 3D diffusivity model. As we are interested in pressure changes only, our modeling approach is simpler and involves a poroelastic diffusion modeling in full space (Rudnicki, 1986). A hydraulic diffusivity of  $D = 0.033 \text{ m}^2/\text{s}$  is found to explain the  $\Delta P_f$  variations at the open section of the main well (Figure 6d). Here we used a rigidity of 1 GPa, a drained and undrained Poisson ratio of 0.25 and 0.3, respectively, and a Biot-Willies constant of  $\alpha = 0.1$ . The model is used to extrapolate into the artesian phase during injection, where no water level measurements were possible.

Induced seismicity was recorded at a borehole geophone in the main hole (three components, 15 Hz, 1,000 Hz sampling rate, clamped at different depths between 1,950 and 3,000 m) and a surface array of five short-period stations in a distance of up to 3 km from the main hole (Haney et al., 2011; Shapiro et al., 2006). The largest 104 induced earthquakes had magnitudes between  $-1.8 \leq M_L \leq 1$  and could be accurately located from both networks. The events occurred between 3.3 and 4.9 km depth near the main well (Figures 6a and 6c). The borehole geophone was very close to the center of the cluster. In total, about 3,040 event arrivals were detected from which 2404 clustered micro-earthquakes were located with magnitudes  $M_L \geq -3.8$  and with a magnitude of completeness of  $M_c \sim -2.75$  (Haney et al., 2011). We use a more conservative limit of  $M_c = -2.3$  (Figure 6e).

The first seismicity occurred when the pore pressure at depth in the main hole reached and exceeded the original level from before 2002 (Figure 6d). We performed simulations to verify whether TDSR can explain the onset and time evolution of the earthquake rate. We assume that  $\mu \Delta P_f$  dominates the Coulomb stress change, where  $\mu$  is the friction coefficient. Our estimated Coulomb stress change thus covers the full experiment from the pumping over the recovery to the injection phase over altogether 1,200 days. As the experiment took so long, it poses a unique opportunity to test stress shadow models.

The stress state at KTB is known to be critical, where small stress perturbations triggers earthquakes (Zoback & Harjes, 1997). Thus, we assume a stationary pre-stress distribution according to Equation 6. The majority of the activity occurred with a distance between 300 and 600 m to the injection point, thus we averaged the TDSR-response function in this distance range and calibrated the resulting curve by the total number of observed earthquakes with magnitude exceeding  $M_c$ . Figure 6f shows the result earthquake rates for  $\delta\sigma/\mu = 0.9, 1.0$ , and  $1.1 \text{ MPa}$  using a tectonic stressing rate of  $\dot{\sigma}_c = 30 \text{ Pa/year}$ . Assuming  $\mu \approx 0.5$ , we estimate slightly larger  $\delta\sigma$ -values as for aftershock sequences. The onset and non-linear increase of the observed seismicity rate are well explained.

### 3.2.3.2. Morsleben

The second example involves the controlled refilling of an about 80 years old, abandoned salt gallery in the Morsleben mine, Germany, in a depth of 300 m below the surface. The salt-cement was backfilled continuously for approximately 182 days, with the exception of weekends and holidays, resulting in periodic variations of thermally induced Coulomb stresses in the roof region of the gallery. The periodic stress variations induced microseismic activity, so-called acoustic emissions in the frequency range of 1–20 kHz. A detailed description of the mine, the salt rock, the seismic monitoring system, and the location and magnitude estimation can be found in Köhler et al. (2009) and Becker et al. (2010). The high-quality catalog of AE events comprises hundreds of thousands of high-quality events which occurred in a confined volume above the backfilled gallery. Coulomb stress changes in the roof region were calculated with a 2D thermo-elastic finite element method using temperature measurements as boundary conditions (Becker et al., 2010). The observed AEs showed a high correlation to positive Coulomb stress changes but also clear stress shadow effects (Becker et al., 2010). Figures 7a and 7b shows a map-view and cross-section of the mine structure together with the seismic network and the AEs. Figure 7c shows the  $\Delta\sigma_c$  changes in the selected rock volume of  $V = 15 \times 15 \times 10 \text{ m} \sim 2,250 \text{ m}^3$  in the southern region as defined in Becker et al. (2010). In this volume,  $\Delta\sigma_c$  changes almost in phase with little spatial variations.

We applied the TDSR model using the modeled  $\sigma_c(t)$ . In contrast to the KTB case, the pre-stress is expected to be subcritical in the salt mine and tectonic stressing is zero. Thus, we assume a subcritical, uniform pre-stress distribution at the starting time, that is,  $\chi(\zeta) = \chi_0 H(\zeta - \zeta_{\min})$ . The susceptibility  $\chi_0$  is determined by the condition

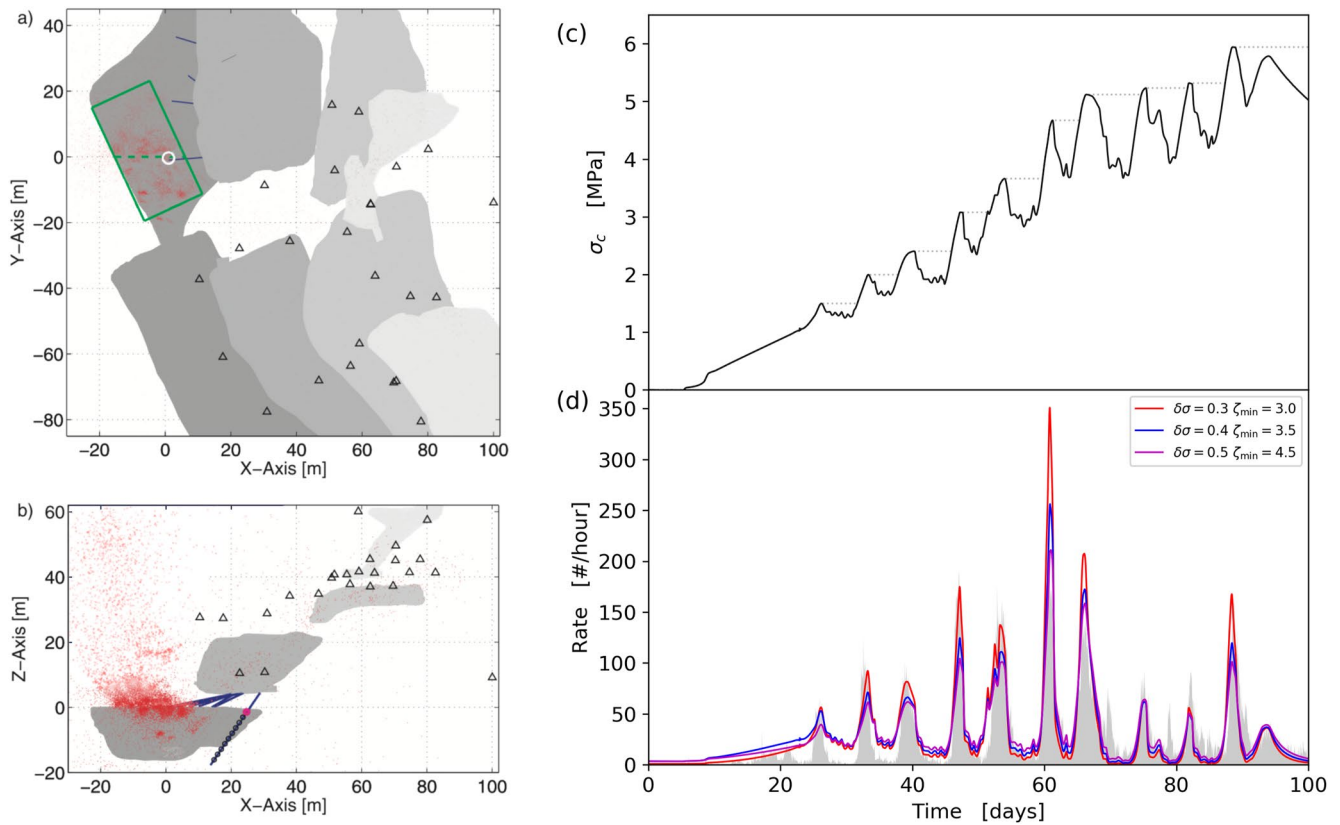


**Figure 7.** (a) Map view and (b) cross-section through the mine structure in Morsleben together with the seismic network of 24 piezoelectric sensors (triangles, sampling rate of 200 kHz) and the acoustic emissions (AEs, red dots) (taken from (Becker et al., 2010)). The deepest gallery in (b) with the intense AE activity was affected by backfilling. The green rectangle in (a) indicates the volume in which AEs were selected for the analysis. The white circle indicates the position of the well where a temperature sensor chain was installed and used to model  $\Delta\sigma_c$ . The blue lines indicate temperature monitoring wells used to model the thermal stress history. (c) shows the Coulomb stress (solid line), where horizontal dashed lines indicate stress shadows. (d) compares the observed AE rates (gray shaded) with TDSR forecasts using different  $\delta\sigma$  and  $\zeta_{\min}$  values (see legend in units of MPa) and  $t_0 = 0.01$  d.

that the total number of the predicted events should equal the observed ones. The remaining model parameters are  $\zeta_{\min}$ ,  $t_0$ , and  $\delta\sigma$ . For simplicity, we set  $t_0 = 0.01$  days but noticed that similar results are obtained for other  $t_0$  values if  $\zeta_{\min}$  is rescaled. Thus, the two parameters  $\zeta_{\min}$  and  $\delta\sigma$  determine the shape of the predicted model rate.

Figure 7d shows the comparison of the observed rates with the model forecasts for three skin parameters,  $\delta\sigma = 0.3$  MPa, 0.4 MPa, and 0.5 MPa, and corresponding  $\zeta_{\min}$ -values. TDSR shows a good fit to the data. The onset and width of the peaks as well as the relative heights of the cycles are well reproduced in all three cases. However, further increasing or lowering  $\delta\sigma$  leads to underestimating or overestimating the rate response to  $\sigma_c(t)$  cycles. Thus, we can conclude that  $\delta\sigma$  is in the range between 0.3 and 0.5 MPa. This is almost the same range as for KTB, while approximately one order larger than the values estimated for aftershock sequences at active tectonic faults.

#### 4. Discussion

Depending on the objective and application, various seismicity models are presently used, including statistical and physics-based models or combinations of both. A recent review of the strength and weaknesses of different models applied to the specific case of the Groningen gas field is given in Kühn et al. (2022). The most popular physics-based seismicity models are the variants of the CF and the RS models, while the ETAS model is the standard statistical model for describing short-term earthquake clustering.

The newly introduced TDSR model can be seen as a generalization of both physics-based CF and RS models. Specifically, the CF model is the limit of TDSR for  $\delta\sigma \rightarrow 0$ , as discussed in Section 2.1. Thus, CF is the special



case of the TDSR for a vanishing skin parameter. Although CF can explain the occurrence of stress shadows (Kaiser effect), its prediction of sudden onsets and ends of total quiescences is not realistic. Furthermore, CF cannot explain Omori-type aftershock activity following sudden stress steps. These shortcomings vanish in the TDSR model with  $\delta\sigma > 0$ .

The relation of the TDSR model to RS is more complicated than to CF. As we have shown in this paper, the analytic and numerical results of RS are identical to the results of the TDSR model for the special case that the initial stress is in steady-state related to background stressing. In particular, the original RS model, as formulated by Dieterich (1994) and Heimisson and Segall (2018), uses the pre-condition  $\dot{\sigma}_c = \text{const} > 0$  and was not developed to study scenarios under  $\dot{\sigma}_c = 0$ . The assumption of initial steady-state conditions leads to a constrained pre-stress distribution. Heimisson et al. (2022) recently extended the RS approach to allow for subcritical starting conditions but still assumes non-zero background stressing rates, manifested in the model parameter  $t_a = A\sigma/\dot{\sigma}_c$ . In contrast, TDSR can be applied to arbitrary initial pre-stress conditions and does not generally require a constant background stressing rate. Simulations with  $\dot{\sigma}_c \approx 0$  can be of particular interest for anthropogenic seismicity occurring in intraplate regions as in the case of our example in Morsleben; or, likewise, after driving a tunnel into a rock mass not subject to tectonic strain and stress rates.

While the predicted seismicity rates are identical for initial steady-state conditions related to  $\dot{\sigma}_c > 0$ , the concepts of both TDSR and RS are very different. The RS model assumes an infinite population of nucleation sites, where slip on each patch is described by a rate- and state-dependent constitutive law derived from friction experiments in the laboratory (Dieterich, 2007). For each of the isolated and non-interacting patches, a simplified spring slider model under friction is used to characterize the nucleation process by an interval of self-driven, accelerated slip, according to the aging law suggested by Ruina (1983). An earthquake is assumed to occur when the slip rate becomes very large or infinity. Finally, the seismicity model only depends on stress changes and not on absolute stress. In contrast, the TDSR model has a direct link to the absolute stress level by assuming that mean time-to-failure  $\bar{t}_f$  is a function of the absolute stress. We use an exponential function (Equation 2) that has been widely used to study subcritical crack growth and brittle failure in geological materials, both under tensional stresses (see review in Atkinson (1984)) and compressional (shear) stresses (Ohnaka, 1983; Scholz, 1968). Thus, it seems enigmatic why RS and TDSR result in the same solutions (for  $\dot{\sigma}_c > 0$ ), despite the contrasting concepts. The underlying reason might be that the RS approach also leads intrinsically to an exponential dependence of the time-to-failure on the absolute stress level. The derivation shown in Appendix B also provides the relation between  $t_0$  and the microscopic and constitutive RS parameters. However, in general, the TDSR approach may also be used with other functional dependencies of  $\bar{t}_f$  on stress, for example, to study the occurrence of tensile cracks.

The simplicity of the TDSR model might offer additional possibilities. By explicitly tracking the stress distribution of sources, possible dependencies of the frequency-magnitude distribution on the stress state can be directly implemented. Particularly, the Gutenberg-Richter  $b$ -value is expected to depend on the absolute stress, with lower values (increased average magnitudes) for higher stress levels (Scholz, 2015). Such relations can be simply implemented and tested in the TDSR approach.

In contrast to the discussed physics-based models, the ETAS model does not rely on stress or stress changes at all. It is a statistical approach to describe short-term clustering of seismicity, particularly aftershock occurrence. For this purpose, it considers a stationary background rate and uses empirical relations to describe clustering: (a) the temporal aftershock decay (Omori-Utsu law), (b) the observed exponential dependence of the aftershock productivity on the mainshock magnitude, and (c) the spatial decay of the aftershock density with distance to the mainshock. Although, the physics-based model also derives all three properties (shown here and in Hainzl et al. (2010)) there are important differences: First, the background rate is additive in ETAS, while it is multiplicative in the physics-based models. It means that the short-term aftershock rate depends only on the mainshock magnitude in the ETAS model, while it also scales with the background rate in TDSR and RS. Second, the aftershock decay is infinite in the ETAS model, while it has a characteristic duration  $t_a = \delta\sigma/\dot{\sigma}_c$  in TDSR, which is better fitting empirical data on average (Hainzl & Christophersen, 2017). Third, the  $c$ -value of the Omori-Utsu relation is not, as in ETAS, a constant but depends on the stress step and is thus space-dependent in the TDSR model. Finally, and maybe most importantly, ETAS only accounts for activation and cannot explain stress shadows. The minimum rate at any location is the tectonic background rate. Despite these unphysical characteristics, the ETAS model mostly outperformed RS implementations in retrospective tests for major aftershock sequences



(Cattania et al., 2018; Woessner et al., 2011). The reason is likely that the physics-based models suffer from the large uncertainties of the mainshock-induced stress changes (Hainzl et al., 2009) and spatial heterogeneities of the physical properties, such as fault density, stress state, fault strength, and fluid pressure, leading to spatial earthquake clustering on small scales (Hardebeck, 2021). Additionally, ETAS accounts for secondary aftershock triggering by smaller magnitude events. However, in the case of anthropogenic seismicity, earthquake-earthquake triggering is less important, and seismicity is largely driven by the time-dependent stress changes related to the human activity. In the latter case, the physics-based models are superior, and ETAS might only be used to explain additional earthquake-earthquake triggering (Kühn et al., 2022).

## 5. Conclusions

Assuming simply an exponential dependence of the mean time-to-failure on the absolute stress, the proposed TDSR model can explain the most important characteristics of seismicity, namely aftershock triggering and stress shadowing. It is a generalization of the deterministic CF model where earthquakes nucleate instantaneously when the strength threshold is exceeded. Furthermore, TDSR leads to the same analytic and numerical solutions as the well-known RS model for the special case of critical initial pre-stress conditions related to a constant background rate, as can be assumed for natural seismicity in general. RS is based on a completely different concept, exploiting a rate- and state-dependent constitutive law derived from laboratory friction experiments. However, TDSR is not limited to initial steady-state conditions and can also simulate seismicity with subcritical initial conditions and zero tectonic stressing. The latter might be of particular interest for applications to human-induced seismicity.

## Appendix A: Analytical Derivations and Simulation Algorithm

### A1. Derivation of the Analytic Solutions

Based on Equation 4 the following cases can be analytically solved.

#### A1.1. Time Evolution for an Initially Uniform $\chi$ in $[\zeta_{\min}, \infty]$

For the case that the initial state is uniformly distribution according to  $\chi(\zeta) = \chi_0 H(\zeta - \zeta_{\min})$  and the volume is loaded with constant stressing rate  $\dot{\sigma}_c$ , the solution of Equation 4 is given by

$$\chi(\zeta, t) = \chi_0 e^{-\frac{\delta\sigma}{t_0\dot{\sigma}_c} \left(1 - e^{-\frac{\dot{\sigma}_c t}{\delta\sigma}}\right)} e^{-\frac{\zeta}{\delta\sigma}} H(\zeta + \dot{\sigma}_c t - \zeta_{\min}) \quad (\text{A1})$$

Inserting this solution in Equation 3 and solving the integral leads to

$$\begin{aligned} R(t) &= \frac{\chi_0}{t_0} \int_{\zeta_{\min} - \dot{\sigma}_c t}^{\infty} e^{-\frac{\delta\sigma}{t_0\dot{\sigma}_c} \left(1 - e^{-\frac{\dot{\sigma}_c t}{\delta\sigma}}\right)} e^{-\frac{\zeta}{\delta\sigma}} e^{-\frac{\zeta}{\delta\sigma}} d\zeta \\ &= \frac{\chi_0 \delta\sigma}{t_0} \frac{1 - e^{-\frac{\delta\sigma}{t_0\dot{\sigma}_c} \left(1 - e^{-\frac{\dot{\sigma}_c t}{\delta\sigma}}\right)}}{\frac{\delta\sigma}{t_0\dot{\sigma}_c} \left(1 - e^{-\frac{\dot{\sigma}_c t}{\delta\sigma}}\right)} \\ &= \chi_0 \dot{\sigma}_c \frac{1 - e^{-\frac{\delta\sigma}{t_0\dot{\sigma}_c} \left(1 - e^{-\frac{\dot{\sigma}_c t}{\delta\sigma}}\right)}}{1 - e^{-\frac{\dot{\sigma}_c t}{\delta\sigma}}} \end{aligned} \quad (\text{A2})$$

#### A1.2. Constant Rate for Constant Loading

Here we consider the case that the rate is constant, that is,  $R(t) = r_0$ , for given stressing rate  $\dot{\sigma}_c$ . In this case, the  $\chi$  distribution is stationary, that is,  $\frac{d}{dt}\chi = 0$ , and Equation 4 leads with  $\frac{d\zeta}{dt} = -\dot{\sigma}_c$  to

$$\frac{\delta \chi}{\delta t} = \dot{\sigma}_c \frac{\delta \chi}{\delta \zeta} \quad (\text{A3})$$

The solution has the general form

$$\chi(\zeta) = c \exp \left( -\frac{\delta \sigma}{t_0 \dot{\sigma}_c} e^{-\frac{\zeta}{\delta \sigma}} \right) \quad (\text{A4})$$

The constant  $c$  is determined by the condition  $R(t) = \int \chi(\zeta) / \bar{t}_f(\zeta) d\zeta = r_0$ , which yields  $c = r_0 / \dot{\sigma}_c$  considering that the integral of  $\exp(-x - a e^{-x})$  is equal to  $\exp(-a e^{-x}) / a$ , which is  $1/a$  for  $x \rightarrow \infty$  and 0 for  $x \rightarrow -\infty$  given  $a > 0$ .

### A1.3. Response to a Stress Step Constant Loading

Here we consider a stress step  $\Delta \sigma_c$  at time  $t = 0$  followed by a constant loading rate  $\dot{\sigma}_{c,a}$  for a source population which was initially at steady state related to a background stressing rate  $\dot{\sigma}_c$ . In this case  $\frac{d\zeta}{dt} = -\dot{\sigma}_{c,a}$  and Equation 4 is equal to

$$\frac{\delta \chi}{\delta t} - \dot{\sigma}_{c,a} \frac{\delta \chi}{\delta \zeta} = -\chi / \bar{t}_f(\zeta) \quad (\text{A5})$$

Given the initial condition  $\chi(\zeta, 0) = \chi_s(\zeta + \Delta \sigma_c)$ , the solution of this equation is given by

$$\chi(\zeta, t) = \frac{r_0}{\dot{\sigma}_c} e^{-\frac{\delta \sigma}{t_0 \dot{\sigma}_{c,a}}} \left[ \left( \frac{\dot{\sigma}_{c,a}}{\dot{\sigma}_c} e^{-\frac{\Delta \sigma_c}{\delta \sigma}} - 1 \right) e^{-\frac{\dot{\sigma}_{c,a} t}{\delta \sigma}} + 1 \right] e^{-\frac{\zeta}{\delta \sigma}} \quad (\text{A6})$$

Inserting this solution in Equation 3 and solving the integral leads to

$$\begin{aligned} R(t) &= \frac{r_0}{t_0 \dot{\sigma}_c} \int_{-\infty}^{\infty} e^{-\frac{\delta \sigma}{t_0 \dot{\sigma}_{c,a}}} \left[ \left( \frac{\dot{\sigma}_{c,a}}{\dot{\sigma}_c} e^{-\frac{\Delta \sigma_c}{\delta \sigma}} - 1 \right) e^{-\frac{\dot{\sigma}_{c,a} t}{\delta \sigma}} + 1 \right] e^{-\frac{\zeta}{\delta \sigma}} e^{-\frac{\zeta}{\delta \sigma}} d\zeta \\ &= \frac{r_0 \delta \sigma}{t_0 \dot{\sigma}_c} \left( \frac{\delta \sigma}{t_0 \dot{\sigma}_{c,a}} \left[ \left( \frac{\dot{\sigma}_{c,a}}{\dot{\sigma}_c} e^{-\frac{\Delta \sigma_c}{\delta \sigma}} - 1 \right) e^{-\frac{\dot{\sigma}_{c,a} t}{\delta \sigma}} + 1 \right] \right)^{-1} \\ &= \frac{r_0 \frac{\dot{\sigma}_{c,a}}{\dot{\sigma}_c}}{\left( \frac{\dot{\sigma}_{c,a}}{\dot{\sigma}_c} e^{-\frac{\Delta \sigma_c}{\delta \sigma}} - 1 \right) e^{-\frac{\dot{\sigma}_{c,a} t}{\delta \sigma}} + 1} \end{aligned} \quad (\text{A7})$$

where it is again considered that the integral of  $\exp(-x - a e^{-x})$  is equal to  $\exp(-a e^{-x}) / a$ , which is  $1/a$  for  $x \rightarrow \infty$  and 0 for  $x \rightarrow -\infty$  given  $a > 0$ .

### A1.4. Response to a Stress Step Without Subsequent Loading

For the specific case of  $\dot{\sigma}_{c,a} = 0$ , the solution of Equation 8 can be achieved by expanding the exponential term  $\exp(-\dot{\sigma}_{c,a} t / \delta \sigma)$  of Equation A7 in a Taylor series and consider the limit  $\dot{\sigma}_{c,a} \rightarrow 0$ .

### A1.5. Change of Stressing Rate

For the case that at  $t = 0$  the stressing rate changes  $\dot{\sigma}_{c,a} \neq \dot{\sigma}_c$ , the solution provided in Equation 9 follows from setting  $\Delta \sigma_c = 0$  in Equation A7.

## A2. Algorithm

The model is implemented by the following algorithm:

1. Discretize stress evolution  $\sigma_{c,i} = \sigma_c(t_i)$  at time steps  $t_i$  ( $i = 1, \dots, N$ ).
2. Initialize the distribution  $\chi_{k,i}$  at  $\zeta_{k,1} \in [Z_1, Z_2]$  ( $k = 1, \dots, M$ ), where  $Z_1 \ll -\delta\sigma$  and  $Z_2 \gg \delta\sigma$  and larger than the maximum stress change ( $\Delta\sigma_{c,\max}$ ) to avoid finite-size effects. For our simulations, for example, we chose  $Z_1 = -Z$  and  $Z_2 = Z$  with  $Z = 20 \cdot \delta\sigma + \Delta\sigma_{c,\max}$ . In the case of initially subcritical stresses, the value of  $Z_2$  should be further increased.
3. Set  $i = 1$ .
4. Calculate total rate  $R_i = \sum_k (\chi_{k,i} / \bar{t}_f(\zeta_{k,i})) \Delta\zeta$ .
5. Update  $\zeta$ -values by  $\zeta_{k,i+1} = \zeta_{k,i} + \sigma_{c,i} - \sigma_{c,i+1}$ .
6. Update  $\chi$ -values by  $\chi_{k,i+1} = \chi_{k,i} - (\chi_{k,i} / \bar{t}_f(\zeta_{k,i})) \cdot (t_{i+1} - t_i)$ .
7. Set  $i = i + 1$  and repeat steps (4)–(7) until  $i = N$ .

A python implementation of TDSR together with the RS and CF model is provided under the open source GitHub project <https://github.com/torstendahm/tdsr>.

## Appendix B: Mean Failure Times in the TDSR and RS Models

The mean failure time for delayed fractures plays a key role in time-dependent brittle deformation and seismicity models. We use an exponential function (Equation 2) that has been widely used to study subcritical crack growth and brittle failure in geological materials, both under tensional stresses (Aktinson, 1984) and compressional (shear) stresses (Ohnaka, 1983; Scholz, 1968), of the form

$$\bar{t}_f = ae^{E/KT} \cdot e^{(S_0 - \sigma_c)/b} = ae^{E/KT + S_0/b} \cdot e^{-\sigma_c/b} \quad (\text{B1})$$

where  $a$  (unit [s]) and  $b$  (unit [Pa]) are constants and  $S_0$  is the strength of the rock. For stress corrosion processes,  $E$  is the activation energy and  $K$  is the Boltzmann constant (Wiederhorn et al., 1980). In our model, we set  $t_0 = ae^{E/KT}$  and  $\delta\sigma = b$ . A key point is that the mean time-to-failure is defined for a source under a given, absolute stress level  $\sigma_c$ , which is assumed constant.

In the RS model, a simplified spring slider model under friction is used. The nucleation process is characterized by an interval of self-driven, accelerated slip, which is used to define the time-to-failure by the time needed until the slip rate becomes very large or infinity. The time depends on constitutive parameters, the initial slip rate  $\dot{\delta}_0$ , and the stress level. Under constant Coulomb stress, the failure time is given by Eqs. A7 and A14 in Dieterich (1994), that is,

$$\bar{t}_f = \frac{A}{H \dot{\delta}_0} = \frac{A}{H} \{\Pi f(\Theta_i)\} \cdot e^{-\sigma_c/A\sigma} \quad (\text{B2})$$

where  $\sigma$  is the effective normal stress, and  $\{\Pi f(\Theta)\}$  is a product of initial state variables. Furthermore,  $H = \frac{B}{d_c} - \frac{k}{\sigma_0}$  with  $A$  and  $B$  constitutive parameters of the friction relation,  $k$  is the effective stiffness of the source patch, and  $d_c$  a characteristic slip distance over which states evolves (Dieterich, 1994). Note that RS assumes that normal stress remains approximately constant, and the product  $A\sigma$  is taken as a model parameter. The solution (B2) is derived assuming that the stress level  $\sigma_c$  is kept constant. However, the derivation of seismicity rates in the RS model finally uses a time-independent solution for  $\bar{t}_f$  for the case of a constant background stressing rate (Heimisson & Segall, 2018).

The forms B1 and B2 can be directly compared. The mean fracture times are equal if  $\delta\sigma = A\sigma$  and  $t_0 e^{S_0/\delta\sigma} = \frac{A}{H} \{\Pi f(\Theta_i)\}$ . It indicates that the mean time-to-failure for RS dependent frictional instabilities has the same form as the functions derived in lab experiments on brittle deformation and brittle failure. This similarity might explain why the TDSR and RS leads to the same analytic solutions for steady-state initial conditions, despite the very different model concepts.

## Data Availability Statement

The article presents a theoretical model, and all simulations are directly based on the corresponding theory. In the case of the real data examples, we used data from published work referenced in the paper. The TDSR model is available as an open source python software tool under <https://github.com/torstendahm/tdsr>, where all examples presented in this paper can be reproduced. The scripts can alternatively be downloaded from Dahm et al. (2022). The seismic catalogs for KTB and Morsleben were published in previous work and is also included in the example files in the GitHub and in Dahm et al. (2022).

## Acknowledgments

We are grateful to the Associate Editor and two anonymous reviewers for their helpful comments and suggestions. We thank Dirk Becker for the processing data of the Morsleben mine application and Jörn Kummerow for providing locations and magnitudes for the KTB pumping and injection experiment. S.H. was supported by the European Unions 2020 research and innovation programme under Grant Agreement Number 8211185, realtime earthquake risk reduction for a resilient Europe (RISE). Open Access funding enabled and organized by Projekt DEAL.

## References

- Atkinson, B. (1984). Subcritical crack growth in geological materials. *Journal of Geophysical Research*, 89(B6), 4077–4114. <https://doi.org/10.1029/jb089ib06p04077>
- Becker, D., Cailleau, B., Dahm, T., Shapiro, S., & Kaiser, D. (2010). Stress triggering and stress memory observed from acoustic emissions records in a salt mine. *Geophysical Journal International*. <https://doi.org/10.1111/j.1365-246X.2010.0464.x>
- Bourne, S., & Oates, S. (2017). Extreme threshold failures within a heterogeneous elastic thin sheet and the spatial-temporal development of induced seismicity within the Groningen gas field. *Journal of Geophysical Research*, 122(12), 10299–10320. <https://doi.org/10.1002/2017jb014356>
- Bourne, S., Oates, S., & Van Elk, J. (2018). The exponential rise of induced seismicity with increasing stress levels in the Groningen gas field and its implications for controlling seismic risk. *Geophysical Journal International*, 213(3), 1693–1700. <https://doi.org/10.1093/gji/ggy084>
- Candela, T., Wassing, B., Ter Heege, J., & Buijze, L. (2018). How earthquakes are induced. *Science*, 360(6389), 598–600. <https://doi.org/10.1126/science.aat2776>
- Cattania, C., Hainzl, S., Wang, L., Roth, F., & Enescu, B. (2014). Propagation of Coulomb stress uncertainties in physics-based aftershock models. *Journal of Geophysical Research*, 119(10), 7846–7864. <https://doi.org/10.1002/2014jb011183>
- Cattania, C., Werner, M. J., Marzocchi, W., Hainzl, S., Rhoades, D., Gerstenberger, M., et al. (2018). The forecasting skill of physics-based seismicity models during the 2010–2012 Canterbury, New Zealand, earthquake sequence. *Seismological Research Letters*, 89(4), 1238–1250. <https://doi.org/10.1785/0220180033>
- Dahm, T., & Becker, T. (1998). On the elastic and viscous properties of media containing strongly interacting in-plane cracks. *Pure and Applied Geophysics*, 151, 1–16. <https://doi.org/10.1007/s000240050102>
- Dahm, T., Hainzl, S., & Dahm, R. A. (2022). Time-dependent stress response seismicity models (TDSR) V. 0.0.6. GFZ Data Services. <https://doi.org/10.5880/GFZ.2.1.2022.002>
- Dieterich, J. (1994). A constitutive law for rate of earthquake production and its application to earthquake clustering. *Journal of Geophysical Research*, 99(B2), 2601–2618. <https://doi.org/10.1029/93jb02581>
- Dieterich, J. (2007). Applications of rate- and state-dependent friction to models of fault slip and earthquake occurrence. *Treatise on Geophysics*, 4, 107–129. <https://doi.org/10.1016/b978-044452748-6.00065-1>
- Dost, B., Ruigrok, E., & Spetzler, J. (2017). Development of seismicity and probabilistic hazard assessment for the Groningen gas field. *Netherlands Journal of Geosciences*, 96(5), s235–s245. <https://doi.org/10.1017/njg.2017.20>
- Grässle, W., Kessels, W., Kumpel, H., & Li, X. (2006). Hydraulic observations from a 1 year fluid production test in the 4000 m deep KTB pilot borehole. *Geofluids*, 6, 8–23. <https://doi.org/10.1029/2007JB005497>
- Grigoli, F., Cesca, S., Rinaldi, A., Malconi, A., Lopez-Comino, J., Westaway, R., et al. (2018). The November 2017 Mw 5.5 Pohang earthquake: A possible case of induced seismicity in South Korea. *Science*, 360(6392), 1003–1006. <https://doi.org/10.1126/science.aat2010>
- Hainzl, S. (2016). Rate-dependent incompleteness of earthquake catalogs. *Seismological Research Letters*, 87(2A), 337–344. <https://doi.org/10.1785/0220150211>
- Hainzl, S., Brietzke, G., & Zoeller, G. (2010). Quantitative earthquake forecasts resulting from static stress triggering. *Journal of Geophysical Research*, 115(B11), B11311. <https://doi.org/10.1029/2010JB007473>
- Hainzl, S., & Christophersen, A. (2017). Testing alternative temporal aftershock decay functions in an ETAS framework. *Geophysical Journal International*, 210(2), 585–593. <https://doi.org/10.1093/gji/ggx184>
- Hainzl, S., Enescu, B., Cocco, M., Woessner, J., Catali, F., Wang, R., & Roth, F. (2009). Aftershock modeling based on uncertain stress calculations. *Journal of Geophysical Research*, 114(B5), 1–12. <https://doi.org/10.1029/2008jb006011>
- Hainzl, S., Sippl, C., & Schurr, B. (2019). Linear relationship between aftershock productivity and seismic coupling in the Northern Chile subduction zone. *Journal of Geophysical Research*, 124(8), 8726–8738. <https://doi.org/10.1029/2019jb017764>
- Haney, F., Kummerow, J., Langenbruch, C., Dinske, C., Shapiro, S., & Scherbaum, F. (2011). Magnitude estimation for microseismicity induced during the KTB 2004/2005 injection experiment. *Geophysics*, 76(6), WC47–WC53. <https://doi.org/10.1190/GEO2011-0020.1>
- Hardebeck, J. L. (2021). Spatial clustering of aftershocks impacts the performance of physics-based earthquake forecasting models. *Journal of Geophysical Research*, 126(2), e2020JB020824. <https://doi.org/10.1029/2020jb020824>
- Heimisson, E. R., Einarsson, P., Sigmundsson, F., & Brandsdóttir, B. (2015). Kilometer-scale Kaiser effect identified in Krafla volcano, Iceland. *Geophysical Research Letters*, 42(19), 7958–7965. <https://doi.org/10.1002/2015GL065680>
- Heimisson, E. R., & Segall, P. (2018). Constitutive law for earthquake production based on rate-and-state friction: Dieterich 1994 revisited. *Journal of Geophysical Research*, 123(5), 4141–4156. <https://doi.org/10.1029/2018JB015656>
- Heimisson, E. R., Smith, J. D., Avouac, J.-P., & Bourne, S. J. (2022). Coulomb threshold rate-and-state model for fault reactivation: Application to induced seismicity at Groningen. *Geophysical Journal International*, 228(3), 2061–2072. <https://doi.org/10.1093/gji/ggab467>
- Helmstetter, A., & Shaw, B. E. (2006). Relation between stress heterogeneity and aftershock rate in the rate-and-state model. *Journal of Geophysical Research*, 111(B7), B07304. <https://doi.org/10.1029/2005JB004077>
- Hyodo, M., Hori, T., & Kaneda, Y. (2016). A possible scenario for earlier occurrence of the next Nankai earthquake due to triggering by an earthquake at Hyuga-nada, off southwest Japan. *Earth Planets and Space*, 68(6). <https://doi.org/10.1186/s40623-016-0384-6>
- Innocente, J. C., Paraskevopoulou, C., & Diederichs, M. S. (2021). Estimating the long-term strength and time-to-failure of brittle rocks from laboratory testing. *International Journal of Rock Mechanics and Mining Sciences*, 147, 104900. <https://doi.org/10.1016/j.ijrmms.2021.104900>
- Kagan, Y., & Jackson, D. (1991). Seismic gap hypothesis: Ten years after. *Journal of Geophysical Research*, 96(B13), 21419–21431. <https://doi.org/10.1029/91JB02210>

- Kagan, Y., & Jackson, D. (1995). New seismic gap hypothesis: Five years after. *Journal of Geophysical Research*, 100(B3), 3943–3959. <https://doi.org/10.1029/94JB03014>
- Köhler, N., Spies, T., & Dahm, T. (2009). Seismicity patterns and variation of the frequency-magnitude distribution of microcracks in salt. *Geophysical Journal International*, 179(1), 489–499. <https://doi.org/10.1111/j.1365-246x.2009.04303.x>
- Kühn, D., Hainzl, S., Dahm, T., Richter, G., & Rodriguez, I. V. (2022). A review of source models to further the understanding of the seismicity of the Groningen field. *Netherlands Journal of Geosciences*, 101(e11), e11. <https://doi.org/10.1017/njg.2022.7>
- Kümpel, H., Erzinger, J., & Shapiro, S. (2006). Two massive hydraulic tests completed in deep KTB pilot hole. *Scientific Drilling*, 3, 40–42. <https://doi.org/10.2204/ioldp.sd.3.05.2006>
- Lohman, R. B., & McGuire, J. J. (2007). Earthquake swarms driven by aseismic creep in the Salton Trough, California. *Journal of Geophysical Research*, 112(B4), B04405. <https://doi.org/10.1029/2006JB004596>
- Mancini, S., Segou, M., Werner, M. J., & Cattania, C. (2019). Improving physics-based aftershock forecasts during the 2016–2017 Central Italy earthquake cascade. *Journal of Geophysical Research*, 124(8), 8626–8643. <https://doi.org/10.1029/2019jb017874>
- Marsan, D. (2006). Can coseismic stress variability suppress seismicity shadows? Insights from a rate-and-state friction model. *Journal of Geophysical Research*, 111(B6), B06305. <https://doi.org/10.1029/2005JB004060>
- Marsan, D., & Ross, Z. E. (2021). Inverse migration of seismicity quiescence during the 2019 ridgecrest sequence. *Journal of Geophysical Research*, 126(3), e2020JB020329. <https://doi.org/10.1029/2020jb020329>
- Matthews, M., Ellsworth, W., & Reasenber, P. (2002). A Brownian model for recurrent earthquakes. *Bulletin of the Seismological Society of America*, 92(6), 2233–2250. <https://doi.org/10.1785/0120010267>
- Miller, S. A., Collettini, C., Chiaraluce, L., Cocco, M., Barchi, M., & Kaus, B. J. P. (2004). Aftershocks driven by a high-pressure CO<sub>2</sub> source at depth. *Nature*, 427(6976), 724–727. <https://doi.org/10.1038/nature02251>
- Nur, A., & Booker, J. (1972). Aftershocks caused by pore fluid flow. *Science*, 175(4024), 885–887. <https://doi.org/10.1126/science.175.4024.885>
- Ogata, Y. (1988). Statistical models for earthquake occurrence and residual analysis for point processes. *Journal of the American Statistical Association*, 83(401), 9–27. <https://doi.org/10.1080/01621459.1988.10478560>
- Ohnaka, M. (1983). Acoustic emission during creep of brittle rock. *International Journal of Rock Mechanics and Mining Sciences & Geomechanics*, 20(3), 121–134. [https://doi.org/10.1016/0148-9062\(83\)91302-5](https://doi.org/10.1016/0148-9062(83)91302-5)
- Ohnaka, M. (2013). *The physics of rock failure and earthquakes*. Cambridge University Press.
- Page, M. T., van der Elst, N., Hardebeck, J., Felzer, K., & Michael, A. J. (2016). Three ingredients for improved global aftershock forecasts: Tectonic region, time-dependent catalog incompleteness, and intersequence variability. *Bulletin of the Seismological Society of America*, 106(5), 2290–2301. <https://doi.org/10.1785/0120160073>
- Passarelli, L., Maccaferri, F., Rivalta, E., Dahm, T., & Abebe Boku, E. (2013). A probabilistic approach for the classification of earthquakes as “triggered” or “not triggered”: Application to the 1975 Krafla diking event followed by the 13th Jan 1976 M 6.2 earthquake on the Tjörnes fracture zone, Iceland. *Journal of Seismology*, 17(1), 165–187. <https://doi.org/10.1007/s10950-012-9289-4>
- Perfettini, H., & Avouac, J.-P. (2004). Postseismic relaxation driven by brittle creep: A possible mechanism to reconcile geodetic measurements and the decay rate of aftershocks, application to the Chi-Chi earthquake, Taiwan. *Journal of Geophysical Research*, 109(B2), B02304. <https://doi.org/10.1029/2003JB002488>
- Reid, H. F. (1911). The elastic rebound theory of earthquakes. *Bulletin of the Department of Geology*, 6, 412–444.
- Richter, G., Hainzl, S., Dahm, T., & Zöller, G. (2020). Stress-based, statistical modeling of the induced seismicity at the Groningen gas field, The Netherlands. *Environmental Earth Sciences*, 79(11), 1–15. <https://doi.org/10.1007/s12665-020-08941-4>
- Roth, F., Dahm, T., & Hainzl, S. (2017). Testing stress shadowing effects at the South American subduction zone. *Geophysical Journal International*, 211(2), 1272–1283. <https://doi.org/10.1093/gji/ggx362>
- Rudnicki, J. (1986). Fluid mass sources and point forces in linear elastic diffusive solids. *Mechanics of Materials*, 5(4), 383–393. [https://doi.org/10.1016/0167-6636\(86\)90042-6](https://doi.org/10.1016/0167-6636(86)90042-6)
- Ruina, A. (1983). Slip instability and state variable friction laws. *Journal of Geophysical Research*, 88(B12), 10359–10370. <https://doi.org/10.1029/jb088ib12p10359>
- Scholz, C. H. (1968). Mechanism of creep in brittle rock. *Journal of Geophysical Research*, 73(10), 3295–3302. <https://doi.org/10.1029/jb073i010p03295>
- Scholz, C. H. (2015). On the stress dependence of the earthquake *b* value. *Geophysical Research Letters*, 42(5), 1399–1402. <https://doi.org/10.1002/2014gl062863>
- Segou, M., & Parsons, T. (2020). The role of seismic and slow slip events in triggering the 2018 M7.1 Anchorage earthquake in the Southcentral Alaska subduction zone. *Geophysical Research Letters*, 47(10), e2019GL086640. <https://doi.org/10.1029/2019gl086640>
- Shapiro, S., Kummerow, J., Dinske, C., Asch, G., Rothert, J., Erzinger, E., et al. (2006). Fluid induced seismicity guided by a continental fault: Injection experiment of 2004/2005 at the German Deep Drilling Site (KTB). *Geophysical Research Letters*, 33(1). <https://doi.org/10.1029/2005GL024659>
- Toda, S., & Stein, R. S. (2022). Central shutdown and surrounding activation of aftershocks from megathrust earthquake stress transfer. *Nature Geoscience*, 15(6), 494–500. <https://doi.org/10.1038/s41561-022-00954-x>
- Utsu, T. (1961). A statistical study on the occurrence of aftershocks. *Geophysical Magazine*, 30, 521–605.
- Vere-Jones, D. (1978). Earthquake prediction – A statistician’s view. *Journal of Physics of the Earth*, 26(2), 129–146. <https://doi.org/10.4294/jpe1952.26.129>
- Wiederhorn, H., Fuller, E., & Thomson, R. (1980). Micromechanics of crack growth in ceramics and glasses in corrosive environments. *Metal Science*, 14(8–9), 450–458. <https://doi.org/10.1179/msc.1980.14.8-9.450>
- Woessner, J., Hainzl, S., Marzocchi, W., Werner, M. J., Lombardi, A. M., Catalli, F., et al. (2011). A retrospective comparative forecast test on the 1992 Landers sequence. *Journal of Geophysical Research*, 116(B5), 1–22. <https://doi.org/10.1029/2010jb007846>
- Zoback, M., & Harjes, H.-P. (1997). Injection-induced earthquakes and crustal stress at 9 km depth at the KTB deep drilling site, Germany. *Journal of Geophysical Research*, 102(B8), 18477–18491. <https://doi.org/10.1029/96jb02814>